

DUNE CONDITIONED FLUID AND PARTICLE FIELD IN A DNS OF SEDIMENT TRANSPORT USING POLYMORPH PARTICLES

Ramandeep Jain

Institute of Fluid Mechanics,
Technische Universität Dresden,
Dresden, Germany
ramandeep.jain@tu-dresden.de

Silvio Tschisgale

Institute für Luft und Kältetechnik Dresden,
01309 Dresden, Germany
silvio.tschisgale@ilkdresden.de

Jochen Fröhlich

Institute of Fluid Mechanics,
Technische Universität Dresden,
Dresden, Germany
jochen.froehlich@tu-dresden.de

ABSTRACT

A direct numerical simulation of sediment transport with a set of particles inspired by a natural sand sample is conducted with a total of 28 types of particles. The generated high fidelity dataset is used to analyze dune-conditioned average fluid and particle fields. The average bed shape, streamwise and wall-normal components of the fluid and particle velocities are reported. The relative particle velocity at four different locations around a dune is also presented. The streamwise velocity of the particle is smaller than the fluid. This difference is larger on the stoss side than on the lee side of a dune. In contrast, the magnitude of the wall-normal component is higher in comparison to that of the fluid. Moreover, it is highest on the lee side. Finally, this study contributes to an improved understanding of the fluid and particle fields around a particle cluster in fluvial system.

1 INTRODUCTION

Recently conducted Direct Numerical Simulations of sediment transport have provided many important insights on particle erosion as well as on particle clustering (Vowinkel *et al.*, 2016; Kidanemariam & Uhlmann, 2017; Jain *et al.*, 2017). These studies, however, represented the solid phase as a set of spherical particles each with the same diameter. Natural sediments, however, are neither perfect spheres nor mono-disperse. In the literature, it is common practice to characterize sediments as triaxial ellipsoids (Zingg, 1935; Smith & Cheung, 2002). The hydrodynamic forces acting on a particle depend on its shape, thereby, influencing its transport in a flow. Additionally, polydispersity influences the sediment transport by means of particle segregation that happens due to various reasons, such as sorting at entrainment, kinetic sieving and equal mobility (Powell, 1998). To overcome this restriction the established simulation methodology was generalized to multi-shape and polydisperse particles and the paper reports on first results obtained with such a particle set. To the knowledge of the authors this simulation is the first DNS with

polymorph particles.

2 NUMERICAL METHOD

The continuous phase is governed by the unsteady, three-dimensional Navier-Stokes equations for incompressible fluids discretized with a second-order finite-volume scheme on a staggered, Cartesian grid. The disperse phase is represented by the equations of motion of all individual particles and coupled to the fluid by an Immersed Boundary Method (IBM) (Tschisgale *et al.*, 2018). This allows simulation of mobile particles with spatially resolved geometry. For particle-particle interaction, a new impulse-based collision model was developed accounting for all forces acting during a collision, such as normal contact force, tangential frictional forces, and lubrication forces.

3 COMPUTATIONAL SETUP

The computational domain of size $L_x \times L_y \times L_z = 108D_{av} \times 23D_{av} \times 36D_{av}$ was discretized with $1944 \times 414 \times 648$ equidistant cells, where D_{av} is the mass weighted average particle diameter defined in Eq. (1) below. The channel is periodic in streamwise (x) and spanwise (z) direction and is considered with a free-slip condition at the top and a no-slip condition at the bottom wall and at the particle surfaces. The bottom of the domain is constituted by a plane wall located at the wall-normal coordinate $y = 0$. On top of it 6747 spherical particles of diameter D_{av} are positioned in a hexagonal pattern. Subsequently, the wall-normal position of these particles is varied by a random displacement Δy_p , within the range $-0.5D_{av} < \Delta y_p < 0.5D_{av}$ as introduced in Jain *et al.* (2017).

Additional to the 6747 fixed particles, the mobile sediment was composed of 42650 mobile particles of various shapes and sizes. Their geometries and equivalent diameters were determined according to the sand sample of Smith and Cheung Smith & Cheung (2002). These authors measured the longest axis a , intermediate axis b , and smallest

Re_b	Re_τ	$D_{av}/\Delta x$	H/D_{av}	D_{av}^+	Δx^+	ρ_p/ρ_f	Fr	Sh/Sh_c	$t_{in} U_b/H$	$T_{av} U_b/H$
3432	343	18	17.6	19.5	1.08	2.55	1.26	5.62	175	270

Table 1. Dimensionless numbers characterizing the simulation. H : clear water height, Re_τ : friction Reynolds number, Δx : cell size of numerical grid, Fr : Froude number, ρ_p : particle density, ρ_f : fluid density, Sh : Shields number built with D_{av} , t_{in} : time marking the start of the averaging procedure, T_{av} : period over which dune-conditioned averaging is performed.

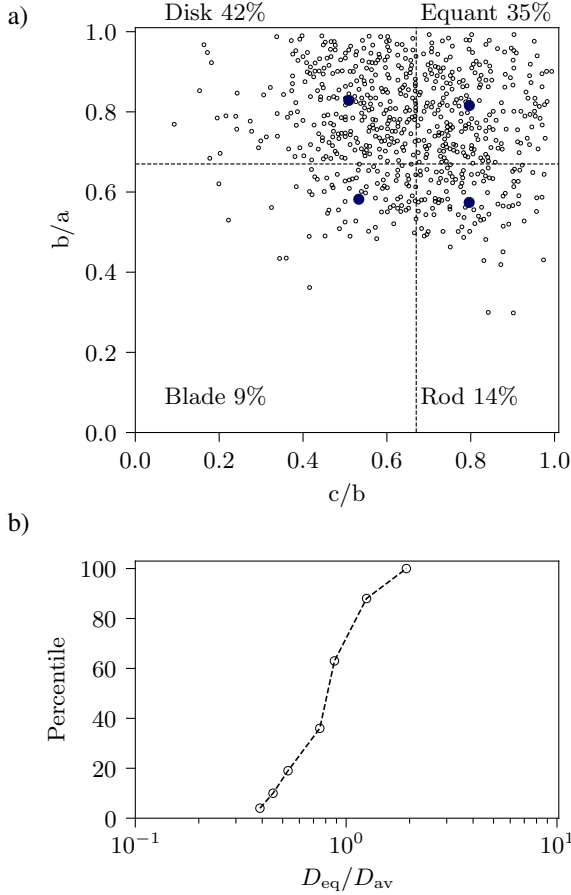


Figure 1. Definition of mobile particles used in the present simulation. a) Ratio of smallest axis to intermediate axis plotted against the ratio of intermediate axis to longest axis. Black circles represent the particles measured in Smith & Cheung (2002). Dark blue dots represent the ratios used in this simulation. b) Sieve curve representing the particle size distribution of Smith & Cheung (2002) also used in the present simulation. The percentile is defined as the total mass of particles finer than a given diameter.

axis c , of 880 particles with different equivalent diameters and plotted them according to the definition of Zingg (1935) as shown in Fig. 1a. To define the set of particles used in the present DNS, the particle shapes falling in each quadrant were averaged to provide one shape representing that quadrant. These 4 shapes are marked as dark blue dots in Fig. 1a. For constant particle density the mass-weighted average is equivalent to the volume weighted average

$$D_{av} = \frac{1}{V_t} \sum_{D_{eq} \in \mathbb{S}} V_{D_{eq}} D_{eq}, \quad (1)$$

where D_{eq} is the diameter of a volumetrically equivalent sphere. Here, V_t is the total volume of the solid phase and $V_{D_{eq}}$ is the volume of particles with equivalent diameter D_{eq} .

The set of equivalent diameters of the particles at Ehukai beach was measured to be $\mathbb{S} = \{0.55 \text{ mm}, 0.63 \text{ mm}, 0.74 \text{ mm}, 1.05 \text{ mm}, 1.24 \text{ mm}, 1.76 \text{ mm}, 2.72 \text{ mm}\}$. The weighted average of Eq. (1) gives $D_{av} = 1.4 \text{ mm}$. Normalization with D_{av} yields $\mathbb{S} = \{0.39D_{av}, 0.45D_{av}, 0.53D_{av}, 0.75D_{av}, 0.88D_{av}, 1.25D_{av}, 1.93D_{av}\}$. In the present simulation each particle size has the same mass percentile as the corresponding size in the natural sediment of Smith & Cheung (2002). As a result, there is a total of 28 types of particles - 4 different shapes, and 7 different sizes.

These particles were initially placed at random positions in space and were allowed to fall freely in vacuum until they come to rest. Afterwards, the fluid was introduced with the streamwise flow driven by imposing a constant flow rate via an additional volume force. The dimensionless numbers characterizing the flow are provided in Tab. 1. The friction velocity, u_τ , required to define some of these parameters was estimated as $\sqrt{\tau_w/\rho_f}$ by calculating the total shear stress τ_w at the sediment-water interface $y = H_{sed}$ defined below. The total shear stress is obtained from momentum balance with volume force driving the flow. For this value the critical Shields number is $Sh_c = 0.035$ when using D_{av} .

4 Methodology

An instantaneous snapshot of the simulation is shown in Fig. 2. To calculate the height of the sediment bed a porosity field $\phi(\mathbf{x}, t)$ is defined such that $\phi(\mathbf{x}, t) = 1$ if the Euler cell at position $\mathbf{x} = (x, y, z)^T$ is fully occupied by the fluid and 0 if it is fully occupied by a particle. Following the recommendations of Kidanemariam & Uhlmann (2017) the instantaneous height of the sediment bed as a function of the streamwise coordinate x is then defined as the elevation where the spanwise averaged porosity equals 0.9, i.e.

$$h_s(x, t) = y |_{\langle \phi \rangle_z = 0.9}. \quad (2)$$

Capart & Fraccarollo (2011) employed a similar threshold value of 0.92 to define the top of the bed-load transport layer. The fluid-sediment interface according to Eq. (2) at many different times is shown in Fig. 3a with the color of the lines representing time. A vertical shift was added to the sediment bed height for clarity and to avoid overlap of the lines. The average sediment-water interface H_{sed} is then obtained by averaging $h_s(x, t)$ in streamwise direction and over time. Furthermore, the spatial fluctuations in the spanwise averaged sediment bed height are determined as

$$h'_s(x, t) = h_s(x, t) - \langle h_s \rangle_x(t). \quad (3)$$

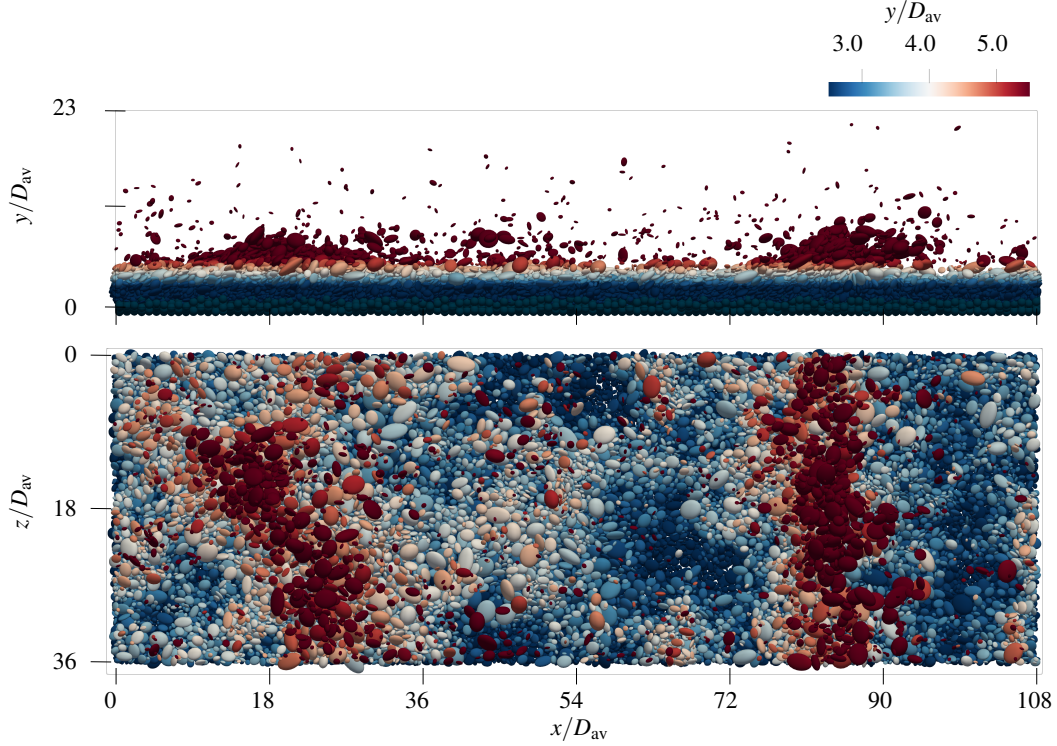


Figure 2. A snapshot of the particles in the simulation at $t = t_{in}$. The particles are colored according to the wall normal position of their center.

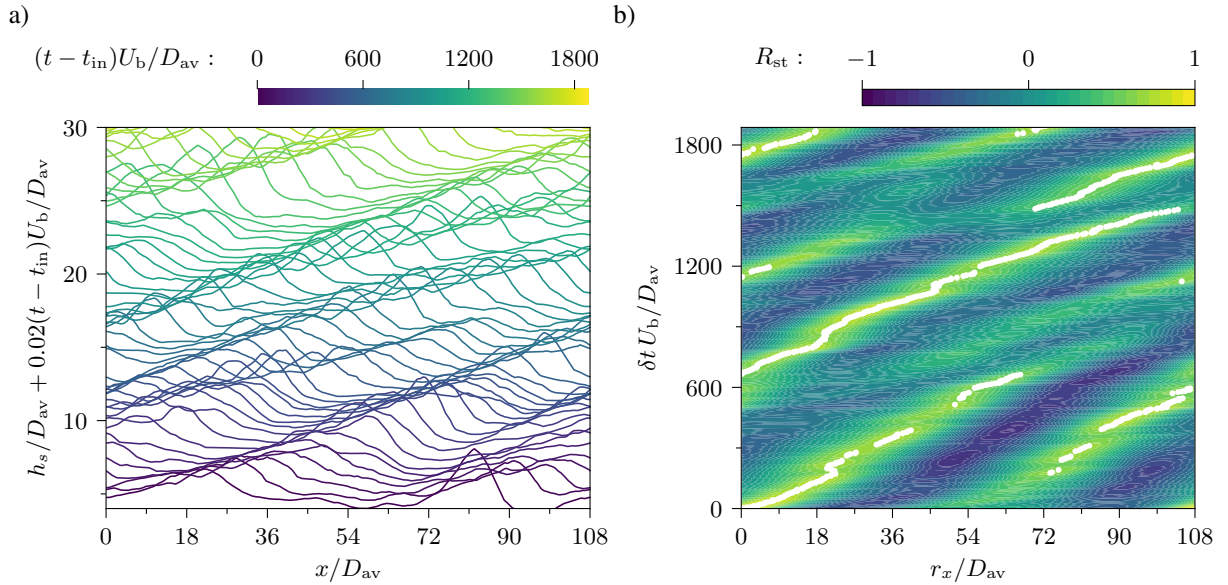


Figure 3. The change in sediment bed height h_s over the time. The y-axis of the profiles is shifted according to the time instant of the profiles for clarity. The colors of the lines correspond to their time as shown in the color bar on the top. a) The original sediment bed profiles h_s . b) The space-time correlation R_{st} .

Based on h'_s from Eq. (3) the space-time correlation function $R_{st}(r_x, \delta t)$ can be defined as

$$R_{st}(r_x, \delta t) = \frac{\langle h'_s(x, t_{in}) h'_s(x + r_x, t_{in} + \delta t) \rangle_x}{\sqrt{\langle h_s'^2(x, t_{in}) \rangle_x \langle h_s'^2(x + r_x, t_{in} + \delta t) \rangle_x}}, \quad (4)$$

where r_x and δt are lags in space and time, respectively. Such a function provides the information on how a bed form

propagates in time (Nikora *et al.*, 1997; Coleman & Nikora, 2011; Kidanemariam & Uhlmann, 2017). Eq. (4) was evaluated yielding the result shown in Fig. 3b.

It can be seen that the streamwise location r_x^m corresponding to the maximum value of R_{st} changes with respect to δt . The values $r_x^m(\delta t)$ are now used to perform the conditional averaging (Kidanemariam, 2016). For this purpose,

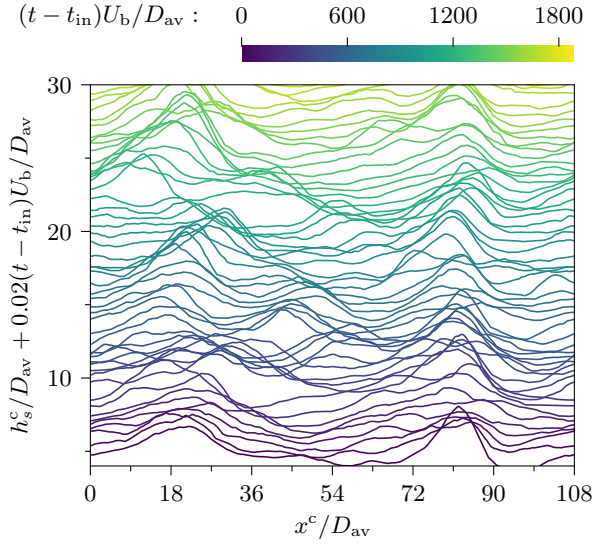


Figure 4. The space-time plots of the dune-conditioned sediment bed profiles h_s^c .

a shifted coordinate x^c is introduced with

$$x^c = x - t_x^m \quad (5)$$

and the upper index c is used for all dune-conditioned quantities. The fluid-bed interfaces shown in Fig. 3a are again drawn in Fig. 4 after the coordinate shift according to Eq. (4). All particle and fluid fields are transformed accordingly while accounting for the periodicity of the computational domain. No transformation is carried out in the spanwise and wall-normal direction. The conditionally time-averaged fluid fields are assessed by

$$\langle \theta \rangle^c(x^c, y) = \frac{1}{T_f} \frac{1}{V_f} \int_{t_{in}}^{t_{in}+T_{av}} \int_{V_0} \phi^c(\mathbf{x}^c, t) \theta^c(\mathbf{x}^c, t) dV dt, \quad (6)$$

where θ is any fluid quantity, t_{in} is the time when averaging starts, T_{av} is the averaging period, and $T_f V_f = \int_{t_{in}}^{t_{in}+T_{av}} \int_{V_0} \phi^c(\mathbf{x}^c, t) dV dt$. Here, V_f is the part of the volume V_0 occupied by fluid and T_f is the total time when the volume V_0 was occupied by fluid even briefly. According to Jain *et al.* (2017), an averaging volume $V_0 = 4\Delta x \times 4\Delta y \times L_z$ is used. Such an averaging procedure is known as intrinsic averaging (Nikora *et al.*, 2013). The particle-related fields are calculated by converting the discrete information to a continuum field at an instant t using

$$\theta_p(\mathbf{x}, t) = \sum_{i=1}^{N_{p,mob}} \gamma^i(\mathbf{x}, t) \theta_p^i(t). \quad (7)$$

with γ^i the clipping function which returns all the cells occupied by the i^{th} particle and θ_p^i any physical quantity of the i^{th} particle. Then, the same operation as in Eq. (4) is applied to determine the dune-conditioned particle related fields.

5 Dune-conditioned fluid and particle fields

The streamwise and wall-normal components of the dune-conditioned fluid and particle velocities, are shown in Fig. 5. The dune-conditioned sediment-fluid interface is indicated with a thick white line shown in all the sub-figures. Two distinct dunes can be seen at $x^c \approx 17D_{av}$ and $x^c \approx 81D_{av}$. The latter is the more prominent one. Kidanemariam & Uhlmann (2017) observed one particle cluster in a simulation with a computation domain as long as the one used in the present case considering monodisperse spheres at a different Shields number. The length of the computational box used here is larger than the minimum size required for pattern formation in the present case.

It can be noticed that the fluid fields, Fig. 5a and 5b, are significantly modulated due to the underlying sediment bed. The velocities in both directions are strongly correlated to the form of the bed. As is expected, the mean fluid and particle velocities are very small below the sediment-fluid interface. Above the interface, however, the fluid velocities exhibit large spatial variations. As the cross section available for the flow reduces on the stoss side of the dune, e.g. $60D_{av} \leq x^c \leq 81D_{av}$, the streamwise fluid velocity increases due to mass conservation. Also, the wall-normal component of the fluid velocity is positive in this region indicating an upward moving fluid. The value of the streamwise and wall-normal mean fluid velocities are observed to be highest in the region above the crest of the dune. On the lee side of the dune, e.g. $82D_{av} \leq x^c \leq 95D_{av}$, the fluid decelerates and moves downwards.

The recirculating flow in the lee side found in many experiments conducted with fixed and impermeable dunes, as reviewed in Best (2005), is not visible here. While studying experimentally the fluid field over a single permeable dune fixed on a permeable bed, Blois *et al.* (2014), however, observed flow fields qualitatively similar to the one obtained in the present simulation. They found that a kind of vertical jet emerges from the pore space of the bed and the dune modifying the flow on the lee side. This was also observed later in the numerical study conducted by Sinha *et al.* (2017). Additionally, the dunes in the present simulation are moving in contrast to the cited studies. In fact the conditionally averaged particle structures are not composed of resting particles but of a highly concentrated fluid particle flow with fairly chaotic behavior.

The particle velocity fields shown in Fig. 5c and 5d exhibit the same behavior as the fluid fields. The particles get lifted up and accelerate on the stoss side of the pattern, whereas they decelerate and get deposited on the lee side of the dune. Above $y = 12D_{av}$ single trajectories are observed with individual particles occasionally moving quite high. These events are rare, though, so that averaging is delicate in this region. Comparing the contour plots of the fluid and particle fields, it can be noticed that the particles have smaller mean streamwise velocity and higher magnitude of the wall-normal velocity compared to the fluid. To best of our knowledge, there is no available experimental study which presents the particle velocity fields of a propagating sediment cluster to compare to.

For a detailed quantitative comparison of the fluid and particle averaged fields, the relative velocities in the streamwise and wall-normal direction are defined as

$$\langle u_r \rangle^c = \langle u_p \rangle^c - \langle u \rangle^c, \quad \text{and} \quad (8a)$$

$$\langle v_r \rangle^c = \langle v_p \rangle^c - \langle v \rangle^c, \quad (8b)$$

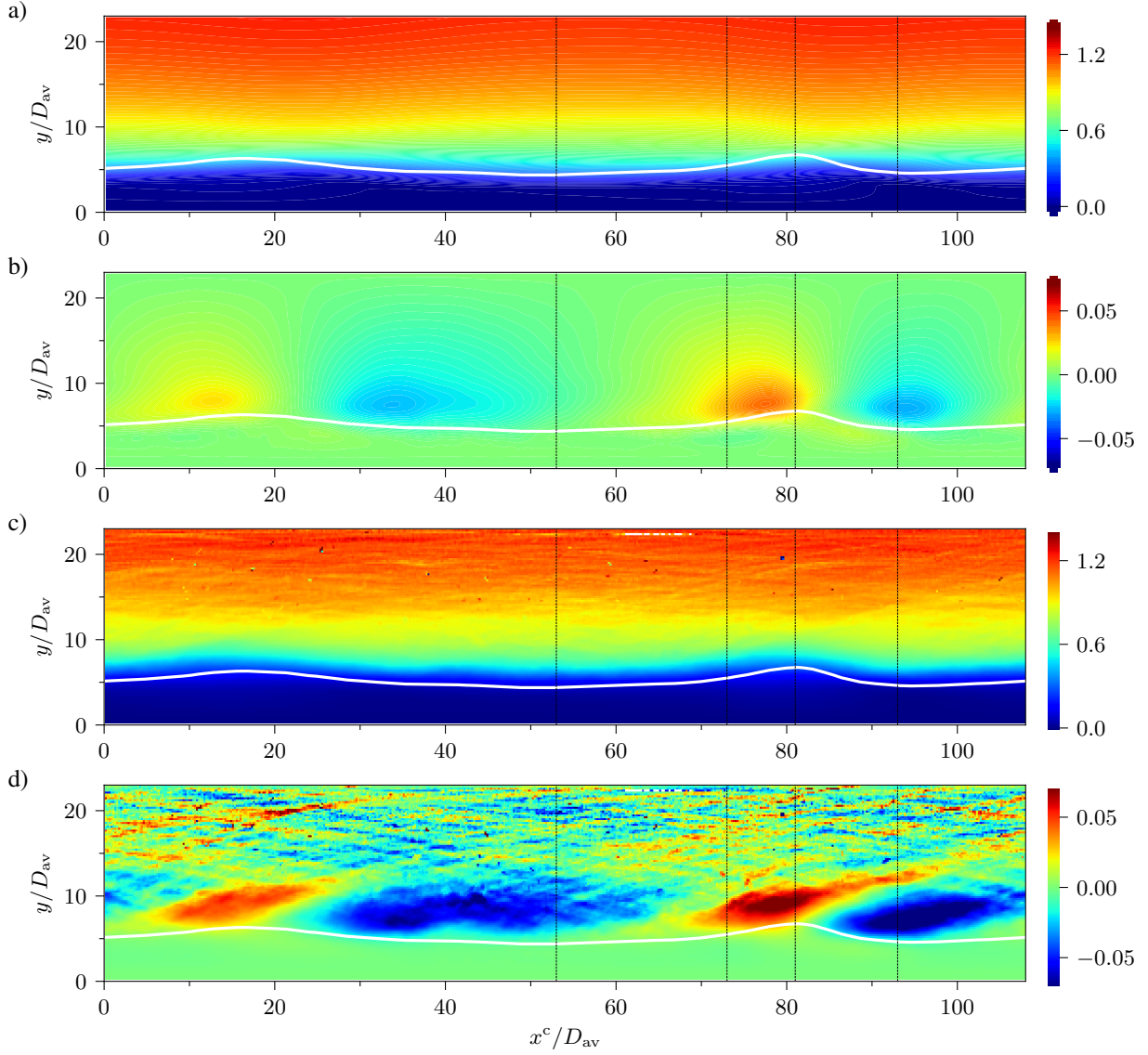


Figure 5. Dune conditioned two dimensional mean fluid and particle fields. a) Streamwise fluid velocity $\langle u \rangle^c / U_b$, b) wall-normal fluid velocity $\langle v \rangle^c / U_b$, c) streamwise particle velocity $\langle u_p \rangle^c / U_b$, and d) wall-normal particle velocity $\langle v_p \rangle^c / U_b$. The thick white line represents the dune-conditioned average sediment bed. The four dotted lines are the positions where fluid and particle velocity fields are quantitatively compared in Fig. 6 below.

respectively. The wall-normal profiles of $\langle u_r \rangle^c$ and $\langle v_r \rangle^c$ at four different locations $x^c = 53D_{av}$, $73D_{av}$, $81D_{av}$, and $93D_{av}$ are drawn in Fig. 6. The graphs are plotted only up to $y = 12.5D_{av}$, where the particle concentration is high enough to get converged statistics. Additionally, the height of the sediment bed at the respective streamwise positions are marked as the horizontal lines on the graphs.

The porosity averaged over time and in x - and z -direction is shown in Fig. 6a. Since the average porosity $\langle \phi \rangle = \langle \phi \rangle_{xzt}$ is almost one for $y > 10D_{av}$, the wall normal profiles of the relative velocities are plotted only up to this height. The particle relative velocity in the streamwise direction is plotted in Fig. 6b. It can be seen that the maximum value of $\langle u_r \rangle^c$ is largest before the dune crest at $x^c = 73D_{av}$ and smallest on the lee side. Additionally, the maximum value occurs at approximately $1D_{av}$ above the sediment bed. Similarly, the wall-normal relative velocity plotted at Fig. 6c can be interpreted. Here, the largest value is on the lee side and on the crest of the dune, whereas the difference is smallest at $x^c = 73D_{av}$. Additionally, the

maximum difference between the magnitudes of the particle and fluid wall-normal velocity occurs approximately $2.5D_{av}$ above the interface. These informations are crucial to understand the turbulence and the exchange of energy between the sediment and the fluid.

Acknowledgements

The authors thankfully acknowledge the computational resources and the support provided by the Center for Information Services and High Performance Computing (ZIH), TU Dresden, Germany. RJ gratefully acknowledge the scholarship provided by the Saxony State Ministry for Higher Education, Research and the Arts, Germany. TS was employed by the Institute of Fluid Mechanics, TU Dresden at the time this study was carried out.

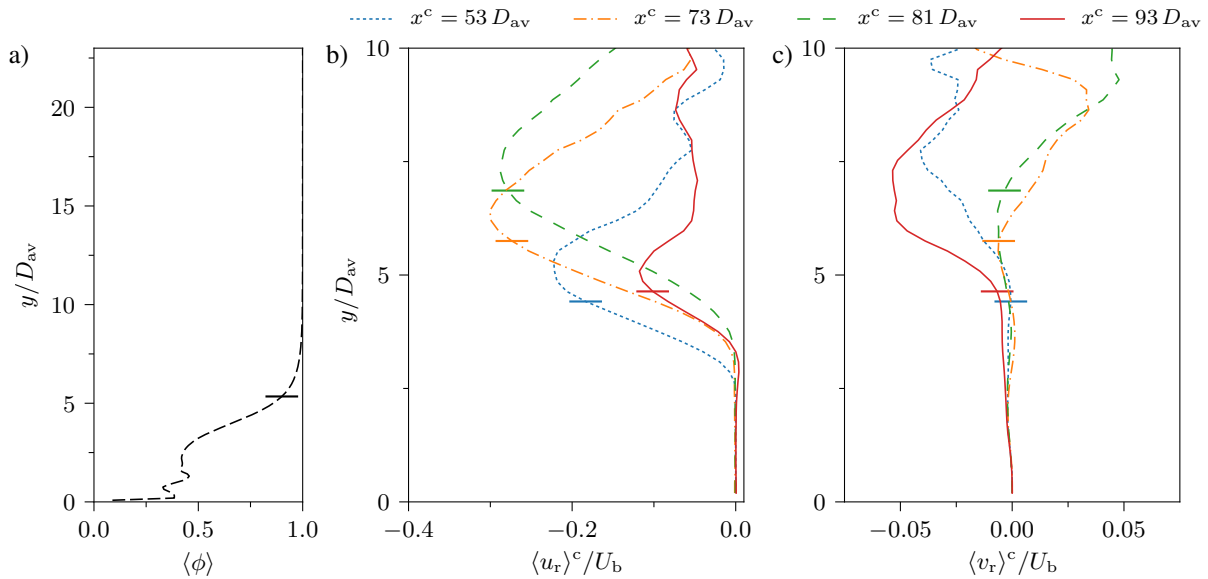


Figure 6. The average porosity and the particle relative velocities at four different locations around a dune. a) The wall normal profile of the porosity averaged over time and in the streamwise and spanwise direction. b) Dune conditioned average streamwise relative velocity, and b) wall-normal relative velocity. The chosen streamwise locations are mentioned in the legend and drawn as dotted lines in Fig. 5. The horizontal lines on the profiles represent the position of the sediment bed at the respective streamwise position.

REFERENCES

- Best, Jim 2005 The fluid dynamics of river dunes: A review and some future research directions. *Journal of Geophysical Research: Earth Surface* **110** (F4).
- Blois, Gianluca, Best, James L., Sambrook Smith, Gregory H. & Hardy, Richard J. 2014 Effect of bed permeability and hyporheic flow on turbulent flow over bed forms. *Geophysical Research Letters* **41** (18), 6435–6442.
- Capart, Hervé & Fraccarollo, Luigi 2011 Transport layer structure in intense bed load. *Geophysical Research Letters* **38** (20).
- Coleman, S. E. & Nikora, V. I. 2011 Fluvial dunes: initiation, characterization, flow structure. *Earth Surface Processes and Landforms* **36** (1), 39–57.
- Jain, Ramandeep, Vowinkel, Bernhard & Fröhlich, Jochen 2017 Spanwise particle clusters in DNS of sediment transport over a regular and an irregular bed. *Flow, Turbulence and Combustion* **99** (3), 973–990.
- Kidanemariam, Aman Ghebremichael 2016 *The formation of patterns in subaqueous sediment*. PhD thesis, KIT Scientific Publishing, Karlsruhe.
- Kidanemariam, Aman G. & Uhlmann, Markus 2017 Formation of sediment patterns in channel flow: minimal unstable systems and their temporal evolution. *Journal of Fluid Mechanics* **818**, 716–743.
- Nikora, Vladimir, Ballio, Francesco, Coleman, Stephen & Pokrajac, Dubravka 2013 Spatially averaged flows over mobile rough beds: Definitions, averaging theorems, and conservation equations. *Journal of Hydraulic Engineering* **139** (8), 803–811.
- Nikora, Vladimir I., Sukhodolov, Alexander N. & Rowinski, Pawel M. 1997 Statistical sand wave dynamics in one-directional water flows. *Journal of Fluid Mechanics* **351**, 17–39.
- Powell, D. Mark 1998 Patterns and processes of sediment sorting in gravel-bed rivers. *Progress in Physical Geography: Earth and Environment* **22** (1), 1–32.
- Sinha, Sumit, Hardy, Richard J., Blois, Gianluca, Best, James L. & Sambrook Smith, Gregory H. 2017 A numerical investigation into the importance of bed permeability on determining flow structures over river dunes. *Water Resources Research* **53** (4), 3067–3086.
- Smith, David A. & Cheung, Kwok Fai 2002 Empirical relationships for grain size parameters of calcareous sand on Oahu, Hawaii. *Journal of Coastal Research* **18** (1), 82–93.
- Tschisgale, Silvio, Kempe, Tobias & Fröhlich, Jochen 2018 A general implicit direct forcing immersed boundary method for rigid particles. *Computers & Fluids* **170**, 285–298.
- Vowinkel, Bernhard, Jain, Ramandeep, Kempe, Tobias & Fröhlich, Jochen 2016 Entrainment of single particles in a turbulent open-channel flow: a numerical study. *Journal of Hydraulic Research* **54** (2), 158–171.
- Zingg, T. 1935 Beitrag zur Schotteranalyse; die Schotteranalyse und ihre Anwendung auf die Glattalschotter (in German). *Schweizerische Mineralogische und Petrographische Mitteilungen* **15** (1), 39–140.